An Ultra-conductive and Patternable 40 nm-thick Polymer Film for Reliable Emotion Recognition

Xiaojia Du[1], Hai Wang[1], Yunfei Wang[2], Zhiqiang Cao[2], Leyi Yang[1], Xiaohu Shi[1], Xiaoxu Zhang[3], Chengzhi He[3], Xiaodan Gu[2], Nan Liu[1]*

[1]Beijing Key Laboratory of Energy Conversion and Storage Materials, College of Chemistry, Beijing Normal University, Beijing 100875, P. R. China.
[2]School of Polymer Science and Engineering, The University of Southern Mississippi, Hattiesburg, MS 39406, USA.
[3]Beijing Advanced Innovation Center for Soft Matter Science and Engineering, Beijing University of Chemical Technology, Beijing 100029, P. R. China.
*E-mail: nanliu@bnu.edu.cn

ABSTRACT

Understanding psychology is an important task in modern society which helps predict human behavior and provide feedback accordingly. Monitoring of weak psychological and emotional changes requires bioelectronic devices to be stretchable and compliant for unobtrusive and high-fidelity signal acquisition. Thin conductive polymer film has been regarded as an ideal interface; however, it is very challenging to be simultaneously balance mechanical robustness and opto-electrical property. Here, we report a 40 nm-thick film based on photolithographic double-network conductive polymer mediated by graphene layer, which concurrently enables stretchability, conductivity and conformability. Photolithographic polymer and graphene endow the film photopatternability, enhance stress dissipation capability, as well as improving opto-electrical conductivity (4458 S cm^{-1} @ > 90% transparency) through molecular rearrangement by π-π, electrostatic interaction and hydrogen bonding. We further apply the film onto corrugated facial skin, monitor the subtle electromyogram, and perform machine learning algorithm to understand complex emotions, indicating the outstanding ability for stretchable and compliant bioelectronics.

INTRODUCTION

With the rapid development of society, there is a growing emphasis on personal health,

particularly in emotion management. Emotions, as the reactions humans experience in response to events or situations, exert a significant influence on our daily lives. (*1-3*). Various technologies were adopted to recognize emotion, including speech signals analysis, facial action coding system based on images, and electrophysiological signals analysis (*2-4*). Of these methods, electrophysiological signals analysis stands out for its precision, sensitivity, and resistance to camouflage. However, the weak and high-fidelity electrophysiological signals acquisition is challenging, which stems from the mechanical mismatches between electronic devices and bio-interfaces, along with the mechanical failure of conducting materials under complex strains (*5, 6*). Such mismatches and failures can severely degrade the transmission of signals, affecting measurement precision in particular situations. For instance, facial electromyography (fEMG) contains rich information on facial muscle activity, health and emotion (*7-9*), and accurate acquisition of fEMG is highly dependent on the well mechanical matching between bioelectronic devices and the corrugated and dynamic facial muscles. Motion artifacts and electrical interference can lead to significant inaccuracies in fEMG recordings, resulting in erroneous or unclear emotion recognition (*10*). This not only hampers the effectiveness of emotion-sensitive applications but also poses a challenge in ensuring reliable human-machine interactions where understanding complex emotional states is crucial.

To construct effective bioelectronic interfaces, materials including metals, conductive polymers, and carbon materials are commonly used (*11-13*). Metal electrodes, known for their superior conductivity, are commonly used in bioelectronics for electrical recording and stimulation (*14*). However, limited by their inherently large modulus and single conductive mechanism, metal electrodes cannot conform well to human skin or tissues. They are prone to breakage under extensive strain and exhibit weak coupling with ionic transport, leading to signal shifts and motion artifacts (*15,16*). Poly(3,4-ethylenedioxythiophene): poly(styrene sulfonate) (PEDOT:PSS), as one of the most important conductive polymers, possesses mixed ionic and electronic conductivity, high optical transmittance, biocompatibility, and ease of processing (*17, 18*). The

integration of PEDOT:PSS with ultraviolet (UV)-sensitive polymers imparts photopatternability, a crucial attribute for customizing its use in bioelectronics, thereby enhancing design versatility (*19-21*). Recently, a monolithic optical microlithographic process was presented by Bao et al. By forming physical crosslinking "double network" with UV sensitive crosslinker, they achieved patternable PEDOT:PSS film with a conductivity of ~ 542 S cm^{-1} (*19*). The incorporation of additional polymers compromises the opto-electrical performance of bioelectrodes. To overcome this challenge, they employed a molecular engineering strategy that utilized a topological supramolecular network. Through a series of complex organic synthesis steps, they achieved a PEDOT:PSS film that not only was patternable but also exhibited enhanced stretchability and conductivity (*21*). While these innovative patterning strategies expand the potential applications for PEDOT:PSS, they also highlight an ongoing challenge: simplifying the micro-fabrication process. The goal is to make it more accessible by using materials that are easier to process, yet without sacrificing the high opto-electrical and mechanical performance required for bioelectronics.

Stable bioelectronic interfaces can be effectively realized through compliant engineering of bioelectrodes (*22-24*). Ultrathin thickness (< 1 μm) of the bioelectrodes benefits the conformal contact with skin and tissues, which can improve charge transfer efficiency and comfort during usage (*25-27*). Graphene, as a representative of carbon materials, possessing exceptional conductivity, high optical transmittance, and atomic level thickness (*28-31*). Lu group has developed graphene interfaces which are highly transparent, fully skin/organs-conformable for electrodermal activity sensing and ambulatory cardiac monitoring (*32, 33*). Our group has reported an ultra-conformal, highly conductive PEDOT:PSS bioelectrode with synergistically enhanced conducting mechano-electrical stability facilitated by the realignment of PEDOT and doping effect enabled by graphene (*34*). By leveraging the benefits of graphene, it is highly possible to achieve a sub-100 nm thick polymer film simultaneously with excellent opto-electrical property, mechano-electrical ability, as well as ease of patterning processing for an effective and stable bioelectronic interface.

Here, we report a 40 nm-thick polymer film as a patternable, stretchable, and compliant bioelectrode, showing an opto-electrical conductivity of 4458 S cm^{-1} @ > 90% transparency, a mechanical stretchability up to 105% strain and ease of photopatternability. This polymer film is consisted of photolithographic double-network conductive polymer (PEDOT:PSS and UV sensitive polyethylene glycol dimethacrylate (PEGDMA)) and graphene layers grown by chemical vapor deposition (CVD) (Fig. 1A). The balance of patternablity, conductivity and stretchability are attributed to the molecular rearrangement of PEDOT:PSS by π-π, electrostatic interaction, and hydrogen bonding with graphene and PEGDMA, along with post-treatment with acid. By tailoring the bioelectrode to fit specific facial locations and effectively dissipate stress, we were able to record subtle fEMG signals for emotion recognition experiments. Together with developing a machine learning algorithm to classify different emotions, we achieved a high accuracy (93%) of emotion recognition, unfolding potentials in psychological research, human-computer interaction, and beyond.

RESULTS

Fabrication and characterization of patternable PEDOT:PSS bioelectrode

To endow PEDOT:PSS simultaneously with photopatternablity, superior opto-electrical property, and stretchability, we engineered a double-network structure reinforced by graphene layers. This double network comprises a conductive PEDOT:PSS network intertwined with a crosslinked PEGDMA network. Such double network imparts water resistance to PEDOT:PSS, making it compatible with photolithography processes that use non-organic solvents. Further integrating with graphene is pivotal: not only do they facilitate the realignment of PEDOT chains through π-π interaction, but also serve as buffer layers for energy dissipation under strain, thereby enhancing the film's mechanical property. This 40 nm thin film was fabricated by following steps: i) preparing photolithographic precursor by mixing PEDOT:PSS with UV sensitive polymer (PEGDMA) ; ii) interfacing the blend with graphene layers; iii) forming the

crosslinked double network; iv) co-patterning the double network and graphene. During this process, a photolithographic PEDOT:PSS film (PLP) and patterned PLP/graphene film (PLPG) were sequentially achieved (fig. S1). Additionally, our co-patterning approach grants design flexibility to PLPG (fig. S2).

In general, pristine PEDOT:PSS film (Pr-P) yielded a conductivity of around 0.1 S cm^{-1}. After the addition of PEGDMA, the conductivity was enhanced to ~ 2.6 S cm^{-1}. This may be due to the reduced insulating PSS shell and closer stacking of PEDOT as the PSS/PEDOT ratio decreased with the increasing of PEGDMA content shown in X-ray photoemission spectroscopy (Fig. 1C, fig. S3A). Interfacing with graphene layers, the conductivity of the entire film reached ~ 450 S cm^{-1}. It is hypothesized that the two orders of magnitude increase in conductivity is attributed to the intrinsically high conductivity of CVD graphene and π-π interaction between graphene and PEDOT. To further enhance the conductivity, PLPG film was post-treated with sulfuric acid (PLPG-S), leading to an ultrathin (~ 40 nm thick) and conductive film (4458 S cm^{-1}), which ranks the highest conductivity reported for PEDOT:PSS based films (Fig. 1C, fig. S3B). In addition, PLPG showed a high transparency over 90% at a wavelength of 550 nm due to the excellent optical transmittance of graphene and ultrathin nature (Fig. 1C). Another advantage for PLPG is the compatibility with photolithography. Tree-shaped PLPG films adhering on the wrist demonstrated remarkable patternability and conformability to skin, maintaining intimate contact during both squeezing and stretching due to the ultrathin thickness (Fig. 1, E to G). Compared to reported patternable PEDOT:PSS, PLPG is ultra-conductive, ultra-thin, and transparent, potentially as a stable, stretchable and compliant bioelectrode (Fig. 1D).
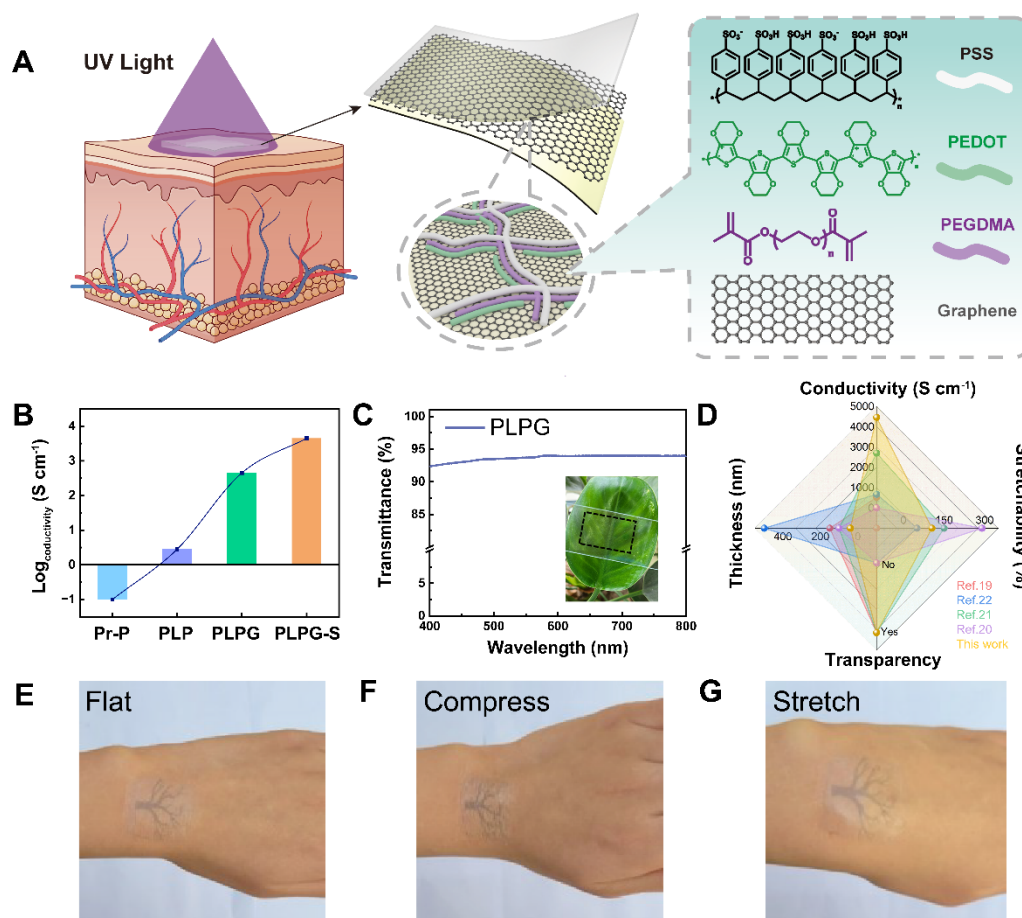
Fig. 1. Fabrication of 40 nm-thick polymer film (PLPG) as a patternable, stretchable and compliant bioelectrode. (**A**) Schematic illustration of PLPG as a UV-patternable bioelectrode. (**B**) Schematic illustration of the fabrication process of patterned PLPG. (**C**) Logarithmic analysis showcasing conductivity characteristics of various PEDOT:PSS films. Pr-P denotes pristine PEDOT:PSS film, PLP denotes photolithographic PEDOT:PSS film, PLPG denotes PLP/graphene film, PLPG-S denotes PLPG film post-treated with acid. Two orders of magnitude sharp increase in conductivity was observed after PLP interfacing with graphene layers. (**D**) Comparison of conductivity, thickness, transparency, and stretchability between PLPG and patterned PEDOT:PSS in references. (**E**) Photo of transparent PLPG on a SEBS substrate. (**F** to **H**) Photos showing a tree-shaped PLPG film on tattoo conformably adhered to flat, compressed and stretched skin.

Mechano-electrical performance of PLPG

To enable PLPG as a patternable, stretchable and compliant bioelectrode, the content of photolithographic polymer was first optimized. Four-probe sheet resistances (R_{sh}) and transmittances at 550 nm were compared on PLP, PLPG and PLPG-S with various weight ratios of PEGDMA vs. PEDOT (1.2, 1.3, and 1.4), labeled as 1.2 w, 1.3 w, and 1.4 w respectively (Fig. 2A and B). With the increase of PEGDMA content, the film conductivity gradually increased and the transmittance slightly decreased, but still remaining above 90% at 550 nm wavelength (Fig. 2C). The mechano-electrical stability with different weight ratios of PEGDMA vs. PEDOT were also investigated (Fig. 2D), displaying that PEGDMA content positively affected film's stretchability. These observations in turn suggested two key functions of PEGDMA: enhancing conductivity and reducing Young's modulus of the film. To illustrate the role of graphene, PLP films with varying numbers of graphene layers after acid post-treatment (denoted as PLP-S with 0-2 G) were compared. The findings revealed that with a higher number of graphene layers, PLPG demonstrated improved mechano-electrical stability (Fig. 2E, fig. S4). Interfacing with bi-layer graphene and applying strain on underlying SEBS substrate, PLPG can maintain conductive up to 105% strain, which exceeded the requirement for bioelectronics. In mechanical durability test, the resistance of 1.4 w PLPG-S remained stable even after 2000 cycles at 30% strain (Fig. 2F). Hence, the optimal composition for PLPG was selected as 1.4 weight ratio of PEGDMA vs. PEDOT, bi-layer graphene and post-treated with sulfuric acid. To illustrate the enhancement of mechano-electrical stability induced by graphene and PEGDMA respectively, atomic force microscope (AFM) imaging was conducted on Pr-P, PLP, and PLPG. When applying 30% strain on SEBS substrates, larger cracks, mostly perpendicular to strain direction, appeared on Pr-P, while smaller cracks appeared after addition of PEGDMA (Fig. 2, G to I). This is probably caused by the enhanced PEDOT polymer chain-slip capability attributed to weakening of Columbic interaction between PEDOT and PSS. As PEGDMA forms hydrogen bonds with PSS, it consequently reduces the Coulombic attraction between the rigid, conjugated backbone of PEDOT and PSS. After interfacing with graphene layers, widths of cracks on PLPG further became smaller and film roughness significantly decreased. Therefore, graphene is

suggested to serve a dual role: an electrical bridging layer to sustain conductivity under strain and a buffer layer to dissipate mechanical stress. Taken together, PEGDMA and graphene co-enhanced the mechano-electrical stability of PLPG, suggesting that micro-structure engineering occurred on PEDOT chains, the major conductive component in PLPG polymer film.
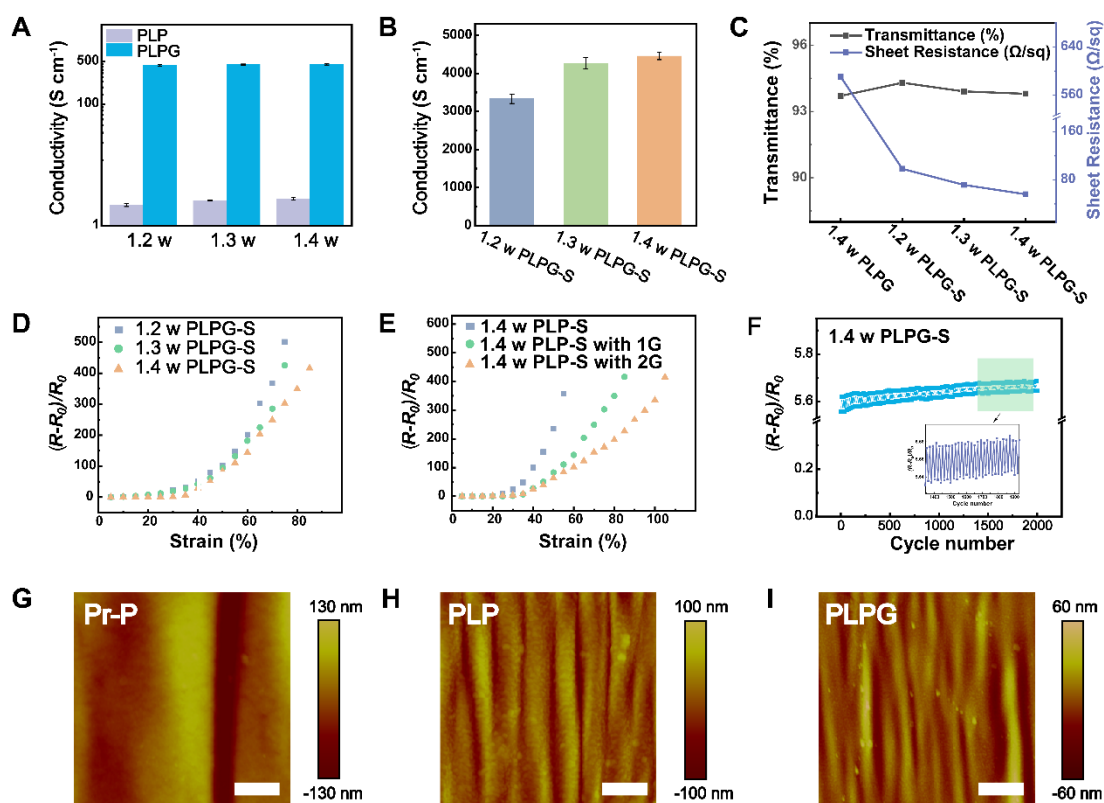

Fig. 2. Mechano-electrical stability of PLPG. (**A** and **B**) Comparison of conductivity between PLP, PLPG before (A) and after (B) sulfuric acid post-treatment with three different weight ratios of PEGDMA vs. PEDOT (1.2, 1.3, 1.4). (**C**) Four-probe sheet resistance (R_{sh}) and transmittance at 550 nm of PLPG films at various PEGDMA proportions. (**D**) Normalized resistance changes of PLPG at various PEGDMA proportions, where strain was applied on underlying SEBS substrate. (**E**) Normalized resistance changes of PLPG-S at various graphene layers (0, 1, 2) upon strain. (**F**) Normalized resistance change of PLPG under cyclic strain (30%) loading. (**G** to **I**) Atomic force microscopy (AFM) images of Pr-P, PLP and PLPG upon 30% strain. Scale bar, 1 μm.

Micro-structure engineering of polymer chain in PLPG

To elaborate the micro-structure in PLPG, we conducted systematic analysis and monitored the molecular packing evolution of PEDOT chains upon interaction with PEGDMA, graphene and sulfuric acid. Grazing-incidence wide angle X-ray scattering (GIWAXS) is a powerful tool to reveal orientation of polymer chains particularly for thin films (*35*). 2D GIWAXS patterns and corresponding 1D curves of Pr-P, PLP, PLPG and PLPG-S films were compared (Fig. 3A, fig. S5). By analyzing (010) peak at around q_z=1.8 Å^{-1}, π–π stacking distance of PEDOT along the in-plane direction can be calculated from Bragg's law (*36*). With the addition of PEGDMA, the π-π stacking distance of PEDOT obviously decreased (Fig. 3C), indicating stronger PEDOT interchain coupling. After adding graphene underneath, the π-π stacking distance further decreased to 3.37 Å, which is an extremely small value for solution-processed PEDOT films. The strong π-π interaction between graphene and PEDOT would contribute to such a close stacking of PEDOT chains along the in-plane direction. Post-treatment of PLPG with sulfuric acid barely affected the π-π distance (3.40 Å), but induced an obvious (100) diffraction peak, corresponding to a denser lamellar packing of PEDOT in the out-of-plane direction (fig. S5). This suggested that the realignment of PEDOT chains could survive the sulfuric acid treatment along with aggregation and crystallization. PSS stacking distances showed similar changing trend as above described in PEDOT (fig. S6). AFM was next used to verify above microstructure evolution of various PEDOT films (Fig. 3B). After addition of PEGDMA and interfacing with graphene layers, PLPG indeed showed interpenetrating networks with surface roughness increased from 1.04 nm in Pr-P to 1.37 nm in PLPG (Fig. 3D). Acid post-treatment had been shown to remove the majority of PSS, further increasing the surface roughness to 1.86 nm. Phase images also clearly revealed micro-structure evolution of PEDOT films from granules to interconnected fibrils, facilitating the transportation of charge carriers with less hopping energy (fig. S7). Thus, PEDOT chains in PLPG tend to densely pack induced by PEGDMA, graphene, and sulfuric acid treatment, leading to improved electrical conductivity.

Raman spectroscopy is another powerful tool for structure fingerprint of thin films (*37*). Here, we studied the conformation changes of PEDOT chains by analyzing the characteristic peak of PEDOT at ~ 1430 cm^{-1}, which is assigned to symmetric $C_\alpha = C_\beta$ stretching vibration of the thiophene ring. After mixing with PEGDMA, this peak blue shifted to ~ 1440 cm^{-1} confirming the strong interchain coupling between PEDOT caused by hydrogen bonding between PEGDMA and PSS (fig. S8). With the increase of PEGDMA, it induced coiled PEDOT chains to extended structures, resulting in slightly red shift of the peak to 1439.6 cm^{-1}. By interfacing with graphene, the vibration peak of PEDOT red shifted to 1436.5 cm^{-1} which was induced by π-π interaction between graphene and PEDOT (Fig. 3E). Actually, this peak can be deconvoluted into two components corresponding with two conformation: the benzoid structure evident at ~ 1445 cm^{-1} and the quinoid structure at ~ 1425 cm^{-1}, which differ in degrees of π-conjugation and π-electron delocalization. As for PLPG both before and after acid treatment, the quinoid part increased continuously, which was consistent with above GIWAXS and AFM results (fig. S8, Fig. 3, A to D). The conformation change of PEDOT from benzoid/coil to quinoid/more linear structures resulted in more effective charge transfer, facilitating the enhancement of conductivity of PLPG. The electronic structure transition within polymer films was also examined by UV-vis-NIR and ESR spectroscopies. Broad absorption bands appeared at ~ 800 nm and ~ 1100 nm, implying the increased charge carriers after interfacing with graphene (fig. S9). ESR spectra demonstrated significantly decreased absorption peak for PLPG, verifying the structure transformation of benzoid to quinoid, corresponding to electronic transportation of polarons to bipolarons (Fig. 3F, fig. S10). As bipolarons are more favorable for charge transportation along the polymer backbone, an enhanced conductivity can be obtained in PLPG.

Overall, micro-structure engineering of polymer chain in PLPG involves three steps: i) PEGDMA aggregates PEDOT chains by forming hydrogen bonding between PSS (Fig. 3G, right top); ii) graphene re-aligns PEDOT chains from benzoid/coil to quinoid/more linear structures via π-π interaction between PEDOT (Fig. 3G, right bottom); iii) acid

treatment promotes PEDOT crystallization via removal of PSS. Thus, PEGDMA functions as an electrostatic interchain coupler of PEDOT, graphene induces a more linear alteration, and acid treatment crystallizes larger PEDOT domains, collectively improving the film's conductivity.
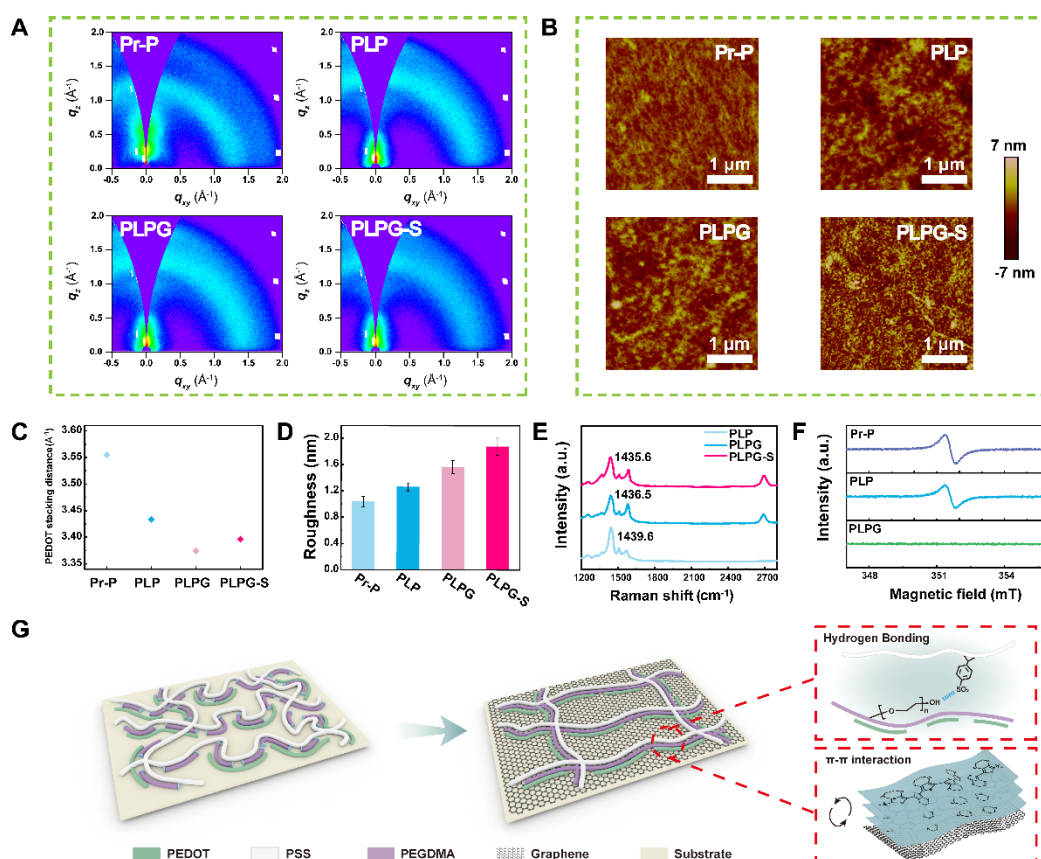

Fig. 3. Micro-structure engineering of polymer chain in PLPG. (**A** to **D**) 2D GIWAXS patterns (A) and AFM images (B) of Pr-P, PLP, PLPG, and PLPG-S with corresponding PEDOT π-π stacking distances (C) and roughnesses (D). (**E**) Raman spectra of PLP, PLPG and PLPG-S. (**F**) ESR spectra of Pr-P, PLP and PLPG. (**G**) Schematic illustration of the micro-structure engineering of PEDOT chains in PLPG. By forming hydrogen bonds between PEGDMA and PSS, PEDOT aggregates with PEGDMA, forming into a semi-double network (right top). Further crosslinking under UV light and interfacing with graphene, PEDOT chains realigned and linked in double network, showing structural transition from benzoid/coil to quinoid/more linear structures via π-π interaction between graphene and PEDOT (right bottom).

Designing of PLPG as a stretchable and compliant bioelectrode

Forming conformal contact on organs/tissues is crucial for stable and high-fidelity electrical signal sensing and modulation in bioelectronics. Due to ultrathin nature of PLPG (~ 40 nm thick), it was able to intimately attach to a human thumb full of wrinkles, indicating the establishment of conformal bio-interface (Fig. 4A). Impedance analysis was conducted by placing a pair of PLPG electrodes on human arm, and lower impedances in all frequencies were achieved compared to commercial Ag/AgCl electrodes (Fig. 4, B and C, fig. S11). After 24 h, the impedance of PLPG electrode at 100 Hz was maintained at ~ 34 kΩ, while Ag/AgCl electrode showed a much higher impedance due to the dehydration of gel, indicating long-term working capability of PLPG electrode. To further analyze the charge transfer at bio-interface, equivalent circuit models were established to represent interfacial impedances at non-compliant and compliant bioelectrodes/skin (fig. S12). Air gaps in between the electrode/skin bio-interface have great influences on interfacial impedance which will produce R_{gap} and C_{gap}. Benefited from the excellent conformability, R_{gap} and C_{gap} at PLPG/skin bio-interface can be ignored, resulting in lower interfacial impedance.

Sensing and modulation of electrical signals are mostly occurred in a dynamic condition, where skin/tissues are being deformed or stretched. In addition to conformability, mechano-electrical stability of bioelectrode serves as another important factor for the establishment of a reliable bio-interface. Because mechanical property of such thin film is difficult to measure, Force curves in AFM were statistically analyzed to compare Young's modulus of PLP, PLPG and PLPG-S (Fig. 4, D and E, fig. S13). Since they are all very thin films transferred onto rigid SiO_2/Si substrates, the measured values reflect mechanical information of both thin films and underlying substrates, thus the values have been normalized with Pr-P for a qualitative comparison. It was observed that addition of PEGDMA softened the film, graphene slightly increased the modulus, and acid treatment decreased the modulus (Fig. 4F). Geometric design is an effective way to improve the stress dissipation ability of thin film electrodes. Three patterns (labeled

as M-1, M-2 and M-3) with same areas were designed and Finite Element Analysis (FEA) was adopted to optimize geometry for stretchable bioelectrodes (Fig. 4G). Upon 10% and 30% strain, a more uniform and smaller stress distribution was obtained in M-3 model. Besides, wider interconnection lines corresponded with better resistances to strain (**fig.** S14). Thus, PLPG with M-3 pattern was fabricated as the compliant and stretchable bioelectrode for following bioelectrical signal sensing.
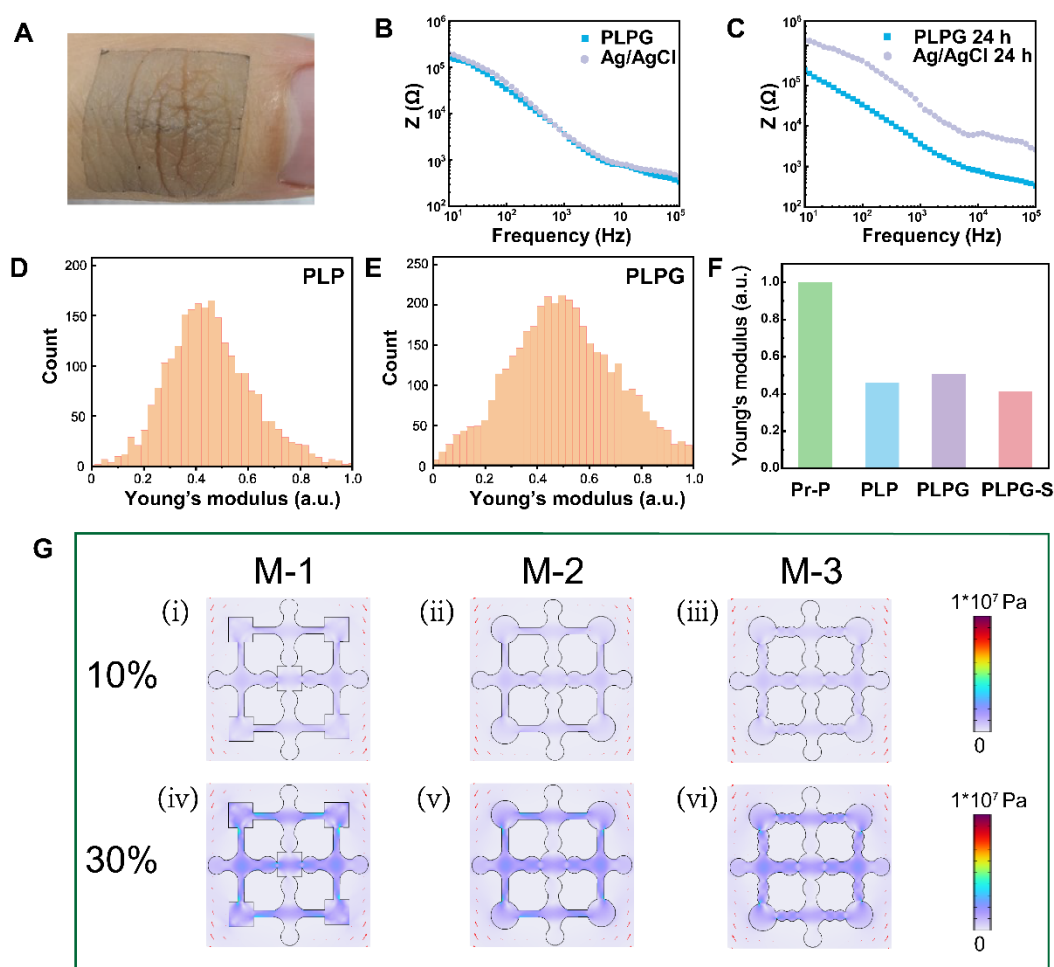

Fig. 4. Designing of PLPG as a stretchable and compliant bioelectrode. (**A**) Photo of PLPG conformably adhered to a human finger. (**B** and **C**) Comparison of interfacial impedance of PLPG and Ag/AgCl electrodes on skin for the first-time use (**B**) and after 24 h in air (**C**). (**D** and **E**) Normalized Young's modulus distribution for PLP, and PLPG. (**F**) Comparison of normalized Young's modulus of Pr-P, PLP, PLPG, and PLPG-S where the value of Pr-P was set as the reference. (**G**) FEA analysis of three electrode patterns at 10% (i-iii) and 30% (iv-vi) strain.

Electrophysiological monitoring with low motion artifact by PLPG

Electrophysiology involves sensing bioelectrical signals from corrugated and dynamic skin/tissues, which can be used for diagnosis of neuromuscular diseases in clinical settings and facilitating the integration of robotic systems in prosthetic applications (*38, 39*). However, motion artifacts severely degrade the accuracy of bioelectrical signals, where noise is mainly generated at the bio-interface between electrode and skin/tissues (*40*). How to reduce motion artifacts ranks as one of the biggest challenges for electrophysiology. To elaborate the advantages of stretchable and compliant PLPG for high-fidelity electrophysiological signal acquisition, PLPGs with M-1 and M-3 patterns were adhered on the forearm for electromyography (EMG) monitoring under motion. An electromechanical vibrator was placed near the electrodes to induce skin motion (Fig. 5, A to C, fig. S15). To quantify the EMG signal quality acquired by various bioelectrodes, signal-to-noise ratios (SNR) were calculated (Fig. 5J). This was done by using the formula: $\text{SNR}=10\times\log_{10}\frac{\text{Signal Power}}{\text{Noise Power}}$. In static status, PLPGs with M-1 and M-3 patterns showed similar SNRs, suggesting that both of them are compliant to skin with stable bio-interfaces. In dynamic status, SNR of PLPG with M-3 pattern was larger than that of M-1 pattern (27 ± 0.8 dB vs. 25 ± 1.5 dB), and obviously better than Ag/AgCl electrode (16 ± 0.9 dB). These indicated that PLPG with M-3 pattern would establish a more stable bio-interface particularly in dynamic condition, thus leading to higher-fidelity electrophysiological signal acquisition.

Baseline deviation was analyzed to further evaluate the electrode resistance to motion artifact. To demonstrate the motion artifact more clearly, EMG signals were presented as time-frequency distribution (spectrogram), where noise and interference are mostly distributed at around 50 Hz. M-3 electrode showed the lowest baseline deviation in both static and dynamic status compared to M-1 and Ag/AgCl electrodes (Fig. 5, D to I). The motion artifacts were quantified by root-mean-squared (RMS), which indicated the fluctuations of the signal over time. In static status, M-3 electrode showed lower RMS noise (25.4 ± 1.9 μV) than M-1 (28.1 ± 3.2 μV) and Ag/AgCl electrode (38.4 ± 3.1 μV).

In dynamic status, though the RMS noise of M-3 electrode increased to ($35.7 \pm 1.8 \, \mu V$), it was 1.2 times smaller than ($43.8 \pm 5.9 \, \mu V$) of M-1 electrode, and 1.5 times smaller than ($53.1 \pm 2.2 \, \mu V$) of Ag/AgCl electrode (Fig. 5K). Overall, PLPG with M-3 pattern herein exhibited the least motion artifact during monitoring of biopotentials, indicating that a stretchable and compliant bioelectrode is very suitable for the deformable and dynamic bio-interface.
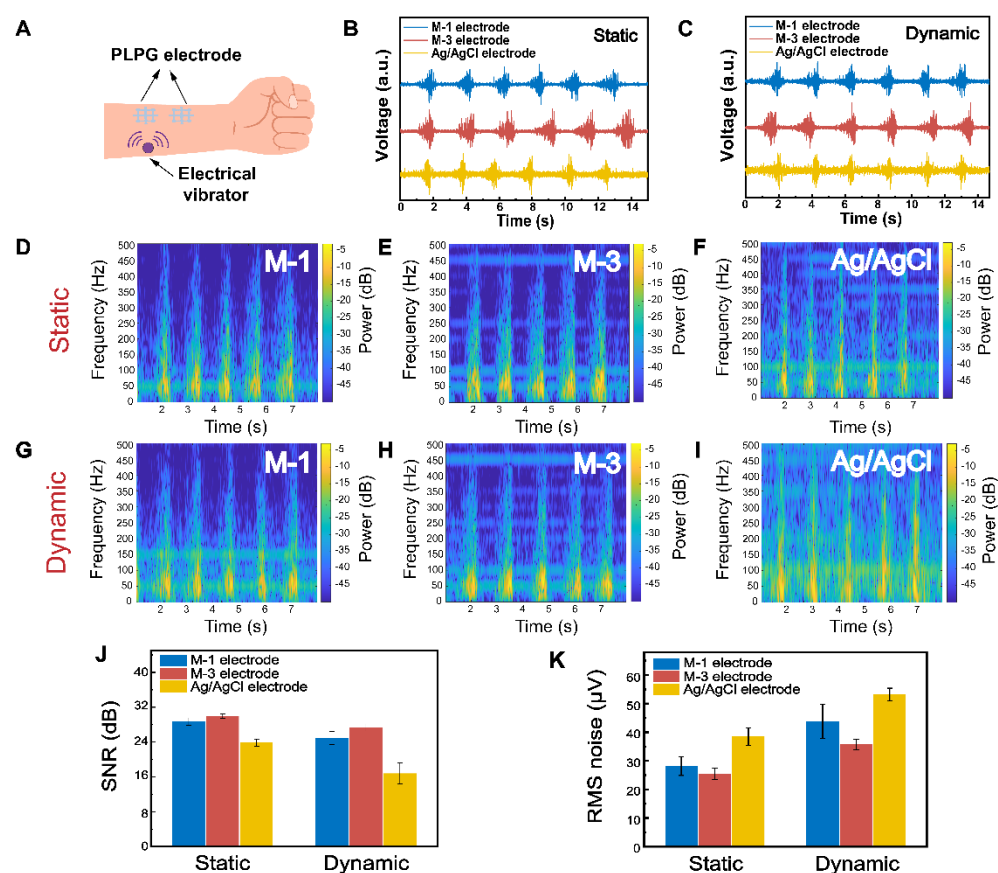

Fig. 5. Electrophysiological monitoring with low motion artifact by PLPG. (A) Recording EMG signals on the skin under vibration induced by an electrical vibrator. (B and C) EMG measured by PLPG with M-1 and M-3 patterns (M-1, M-3), and Ag-AgCl electrodes in static (B) and dynamic (C) conditions. (D to I) Spectrogram analysis of M-1, M-3, and Ag/AgCl electrodes in static (D to F) and dynamic (G to I) status. M-3 electrode showed lower motion artifact at ~ 50 Hz in dynamic status. (J and K) SNR (J) and baseline noise (K) comparison of the three electrodes above in static and dynamic status.

Facial EMG (fEMG) monitoring and machine learning for understanding emotion

Understanding emotion stands as a crucial endeavor in modern society, enabling the anticipation of human actions and furnishing appropriate responses in turn. Common areas of emotion recognition include healthcare, online education, safety education, and human-computer interaction (*41, 42*). For example, patients suffering from Autism Spectrum Disorder (ASD) have difficulties in modulating and processing their own and other's facial expression (*43*). In similar population, facial expression may be hard to perceive visually but can be reliably detected through fEMG. Thus, it is an effective way to understand emotion through monitoring fEMG. However, recording high-fidelity fEMG presents a significant challenge in practical applications, primarily due to inherently weak electrical signals on the face and frequent deformation of the electrode/face bio-interface. These factors critically affect the accuracy rate of recognition.

In general, emotional experiences can be described by two terms: valence (positive or negative) and arousal (intensity of the emotion). Previous studies demonstrated the activity increases in corrugator supercilli in response to negative emotion, while increases in the zygomaticus major in response to positive emotion (*44*). To recognize the emotion of subject, PLPG with M-3 pattern (denoted by PLPG below) electrodes were adhered to corrugator supercilli and zygomaticus to monitor subtle facial activities generated by visual stimuli (Fig. 6, A and B). The pleasant and unpleasant photographs were chosen from standardized stimulus sets from International Affective Picture System (IAPS). Note that the photographs chosen from IAPS are all with high arousal to enhance the visual stimuli. Eight volunteers were involved in this experiment. The volunteer sat in a comfortable position in front of the computer and completed the experiment following the designed pattern (fig. S16). Then, they viewed a set of 30 pleasant photographs for ~ 2 min, and a set of 30 unpleasant photographs for ~ 2 min (see details in Experimental Section). fEMG signals corresponding to these subtle activities of corrugator supercilli and zygomaticus were collected through PLPG.

Acquired signals were preprocessed using moving average filter. For instance, the raw EMG signals and extracted integrated EMG (iEMG) of subject 1 under positive and negative emotion showed specificity, respectively (Fig. 6, C and D). To achieve emotion recognition, a machine learning algorithm was designed to train and classify them (Fig. 6E). Three databases of different emotions containing 71, 46 and 73 were established from 190 fEMG segments in total. After calculating 26 feature values of fEMG from each segment containing different time and frequency domain information, a total of 190×26 feature values from all data sets could be constructed and used in machine learning (Fig. 6, F to H, fig. S17). Positive, negative and neutral emotions were labeled as +1, -1 and 0 so as to carry out machine learning and emotion classification task. For each state, 70% of the data was randomly selected as the training set, and the other 30% data was selected as the test set. The final classification results were obtained by using bidirectional long short-term memory network (BiLSTM) to construct the classification model.

The average prediction of BiLSTM classification model can reach an accuracy of 93.0% (Fig. 6I). The accuracies of correctly predicting negative, neutral, and positive emotions were 86.4%, 100%, and 95.2% respectively. The overall error rate in the predictions across all test samples was 7%. Moreover, the model showed Specificity = 96.3%, Precision = 94.0%, Sensitivity (Recall) = 93.9%, F1 score = 93.8%, MCC = 90.2%, and the Kappa score = 84.2%. These metrics demonstrated the accuracy and reliability of the emotion classification (Fig. 6J). This high accuracy is attributed to the high-quality fEMG signals acquired by PLPG, showing that such stretchable and compliant bioelectrode may overcome the challenges brought from the deformable and dynamic bio-interface, and be applicable in bioelectronics such as fEMG for emotion analysis.
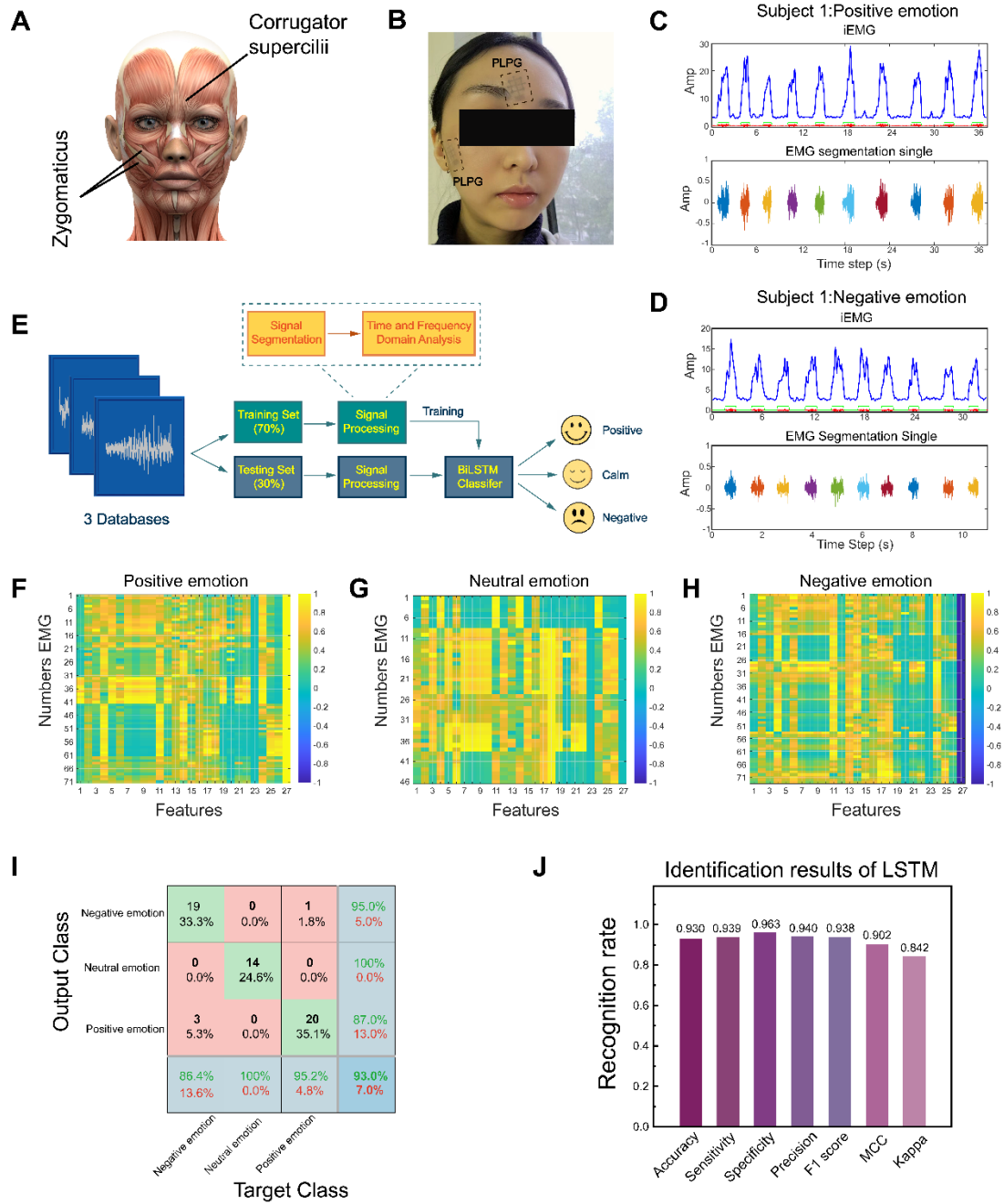
Fig. 6. Facial EMG (fEMG) monitoring by PLPG and machine learning for emotion analysis. (**A**) An image showing the main muscles for emotion expression. (**B**) A photo showing PLPG with M-3 pattern (denoted by PLPG below) electrodes for fEMG acquisition. (**C** and **D**) Representative fEMG signals and corresponding extracted integrated EMG (iEMG) from subject 1 under positive (C) and negative (D) emotions. (**E**) Flow chart of a machine learning algorithm for emotion classification. (**F** to **H**) Thermogram of correlation coefficient of fEMG characteristics in positive (F), neutral (G), and negative (H) emotions. The 27th column is the classification label. (**I**)

Confusion matrix of classification training recognition accuracy. (**J**) Identification results of LSTM.

DISCUSSION

In conclusion, we developed a 40 nm-thick polymer film that can be fabricated as a patternable, stretchable, and compliant bioelectrode. By adopting a polymer-chain engineering strategy, the opto-electrical conductivity of PLPG reached as high as 4458 S cm^{-1} @ > 90% transparency, which ranks the highest conductivity reported for PEDOT:PSS based films. Taking advantage of its patternability, PLPG can be designed into certain patterns, increasing the mechano-electrical stability. Leveraging these metrics, PLPG established a reliable and effective bio-interface thereby enabling motion artifact-less electrophysiological monitoring. In emotion recognition experiment, PLPG demonstrated its capability to monitor subtle fEMG signals with high-fidelity, facilitating the recognition accuracy as high as 93%. Our patternable, stretchable and conformal bioelectrode shows great promise for long-term stability in electrophysiological applications.

MATERIALS AND METHODS

Materials

PEDOT:PSS solution (Clevios PH 1000) was purchased from Han Feng, PVA, PEGDMA (average Mn 750), water-soluble initiator 2-Hydroxy-4'-(2-hydroxyethoxy)-2-methylpropiophenone (Irgacure 2959), Cu foil and SEBS were purchased from Sigma-Aldrich, methylbenzene, sulfuric acid were purchased from Aladdin Industrial Corporation, FS 30 was purchased from Innochem, tattoo paper was purchased from The Magic Touch Ltd., UK.

Fabrication of PLPG electrode

(**i**) Graphene: Large-area graphene was grown on Cu foil (25 μm thick) in a low-pressure CVD system under an atmosphere of 20 sccm H_2 and 35 sccm CH_4 at 1000 °C.

PMMA-assisted wet transfer method was used to transfer graphene onto thin SEBS film. **(ii)** PEDOT:PSS/PEGDMA (PLP) solution: PLP solution contains 1 mL PH1000 (solid content ~ 1.3%, PEDOT content ~ 0.37%), PEGDMA was added with 1.4:1 weight ratio vs. PEDOT; 5 wt% of photoinitiator Irgacure 2959 (vs. PEGDMA), and 1 wt% of Capstone™ FS-30 (vs. PH1000). PLP solution was stirred in dark for 5 h. **(iii)** Patterning of PLPG: PLP solution was spin-coated on graphene mentioned above at 1000 r.p.m. for 100 s and dried at room temperature (RT). PLP film would be later photo-crosslinked by UV exposure through a photomask for 2 min using a Spectrum 100 Precision UV spot curing system (American Ultraviolet, 25 mW cm^{-2}) before rinsing by water. Then, graphene was treated in oxygen (O_2) plasma to remove unexpected part with a protect mask covered on patterned PLP film. As-prepared PLPG film would be further treated with acid by dipping into concentrated sulfuric acid for 10 s before water rinsing and drying to yield PLPG-S film for further testing.

Materials characterization

AFM (Nanoscope-III, Digital Instrument) was used to observe surface morphology. Thickness measurement was performed using a profilometer P7 (KLA Tencor, America). Raman spectroscopy was performed on LabRAM HR Evolution with 532 nm excitation to study the change of PEDOT structure. The laser power was below 1 mW on the sample to avoid laser-induced local heating. Optical transmittance was collected by a SHIMADZU 2450 UV−vis spectrophotometer. XPS was performed using an ESCALAB 250Xi spectrometer with monochromatized Al Kα radiation (incident energy, 1486.6eV) at a pressure of less than 10^{-9} Torr. AFM mapping of Young's modulus were conducted by JPK Nonwizard 4. ESR spectra were collected using a Bruker A300 spectrometer at a microwave frequency of 9.853 GHz. GIWAXS data were obtained using Xenoc Xeuss 2.0 using a copper source. The incidene angle on the sample is around 0.18^0. Electrochemical impedance spectroscopy (EIS) measurement was conducted using a CHI600e electrochemical workstation (CH Instruments). Sheet resistance was measured by a four-point probe method using a Keithley 2636b source meter.

Electrophysiological measurements

(**i**) For EMG measurement, a pair of electrodes were placed on forearm, and reference electrode was placed on the back of wrist. Ag wires and conductive silver paste were used to connect electrodes (M-1 and M-3) to test module. Commercial Ag/AgCl electrodes (3M) were used as reference. To create a dynamic status as arm movement, an electromechanical vibrator was placed near working electrodes (about 2 cm) to induce skin vibration. EMG signals were digitally filtered in MATLAB by a six-order Butterworth filter. Spectrogram for each EMG signal was obtained in MATLAB, the frequency was set as 0-500 Hz.

(**ii**) For fEMG measurement, two electrodes were placed on left corrugator supercilli and zygomaticus respectively as working electrodes. A ground electrode was placed on the mastoid behind the left ear in accordance with published guidelines (*45*). Electrodes were connected to test module with Ag wires. Each subject was asked to sit still in front computer 1 while 3 min of EMG signals were recorded. Then, the subject viewed a set of 30 photographs of pleasant scenes and a set of 30 photographs of unpleasant scenes chosen from IAPS. Photographs were presented in the following ways: affective image for 1.5 s to evoke emotion, gray rectangle image with the same size of affective image for 2 s as the baseline condition. After playing a set of photographs, the subjects filled out a questionnaire to assess how much the subject felt a particular emotion. Then, the subject rested for 3 min before continuing to watch the next set of photographs which were demonstrated with the same procedure. During the demonstration of pictures, fEMG signals were recorded continuously.

(**iii**) Performance of LSTM: Accuracy, Sensitivity, Specificity, Precision, F1 score, Matthew's Correlation Coefficient (MCC), and Kappa were used to evaluate the model. These metrics are defined in terms of true-positive (TP), false-positive (FP), false-negative (FN), and true negative (TN). And they are described as the following formulas:

$$\text{Accuracy} = \frac{\text{TN+TP}}{\text{TN+TP+FN+FP}}$$

$$\text{Sensitivity (Recall)} = \frac{\text{TP}}{\text{TP+FN}}$$

$$\text{Specificity} = \frac{TN}{TN+FP}$$

$$\text{Precision} = \frac{TP}{TP+FP}$$

$$\text{F1 Score} = 2 \times \frac{\text{precision} \times \text{recall}}{\text{precision} + \text{recall}}$$

$$\text{MCC} = \frac{TP \times TN - FP \times FN}{\sqrt{[(TP+FP) \times (FN+TN) \times (FP+TN) \times (TP+FN)]}}$$

Supplementary Materials

This PDF file includes:
Figs. S1 to S17

REFERENCES AND NOTES

1. Y. Jiang *et al.*, A universal interface for plug-and-play assembly of stretchable devices. *Nature* **614**, 456-462 (2023).
2. Y. Wang *et al.*, Skin bioelectronics towards long-term, continuous health monitoring. *Chem. Soc. Rev.* **51**, 3759-3793 (2022).
3. S. Yang *et al.*, Stretchable surface electromyography electrode array patch for tendon location and muscle injury prevention. *Nat. Commun.* **14**, 6494 (2023).
4. W. Zhou *et al.*, Soft and stretchable organic bioelectronics for continuous intraoperative neurophysiological monitoring during microsurgery. *Nat. Biomed. Eng.* **7**, 1270-1281 (2023).
5. Y. Fang *et al.*, Dissecting Biological and Synthetic Soft–Hard Interfaces for Tissue-Like Systems. *Chem. Rev.* **122**, 5233-5276 (2022).
6. J. Sivasundarampillai *et al.*, A strong quick-release biointerface in mussels mediated by serotonergic cilia-based adhesion. *Science* **382**, 829-834 (2023).
7. L. Shu *et al.*, A Review of Emotion Recognition Using Physiological Signals. *Sensors* **18**, 2074 (2018).
8. Y. Golland, A. Hakim, T. Aloni, S. Schaefer, N. Levit-Binnun, Affect dynamics of facial EMG during continuous emotional experiences. *Biol. Psychol.* **139**, 47-58 (2018).
9. Y. Wang *et al.*, All-weather, natural silent speech recognition via machine-learning-assisted tattoo-like electronics. *npj Flexible Electron.* **5**, 20 (2021).
10. E. Farago, D. MacIsaac, M. Suk, A. D. C. Chan, A Review of Techniques for Surface Electromyography Signal Quality Analysis. *IEEE Rev Biomed Eng* **16**, 472-486 (2023).
11. Y. Qiang *et al.*, Transparent arrays of bilayer-nanomesh microelectrodes for simultaneous electrophysiology and two-photon imaging in the brain. *Sci. Adv.* **4**, eaat0626 (2018).
12. T. Zhou *et al.*, 3D printable high-performance conducting polymer hydrogel for

all-hydrogel bioelectronic interfaces. *Nat. Mater.* **22**, 895-902 (2023).

13. Y. Lu *et al.*, Stretchable graphene–hydrogel interfaces for wearable and implantable bioelectronics. *Nat. Electron.* (2023). https://doi.org/10.1038/s41928-023-01091-y

14. W. Ouyang *et al.*, A wireless and battery-less implant for multimodal closed-loop neuromodulation in small animals. *Nat. Biomed. Eng.* **7**, 1252-1269 (2023).

15. N. Wu *et al.*, Electrode materials for brain–machine interface: A review. *InfoMat* **3**, 1174-1194 (2021).

16. A. Mazzotta, M. Carlotti, V. Mattoli, Conformable on-skin devices for thermo-electro-tactile stimulation: materials, design, and fabrication. *Mater. Adv.* **2**, 1787-1820 (2021).

17. X. Du, L. Yang, N. Liu, Recent Progress on Poly(3,4-Ethylenedioxythiophene):Poly(Styrenesulfonate) Bioelectrodes. *Small Sci.* **3**, 2300008 (2023).

18. L. V. Kayser, D. J. Lipomi, Stretchable Conductive Polymers and Composites Based on PEDOT and PEDOT:PSS. *Adv. Mater.* **31**, 1806133 (2019).

19. Y.-Q. Zheng *et al.*, Monolithic optical microlithography of high-density elastic circuits. *Science* **373**, 88-94 (2021).

20. M. Yang *et al.*, Robust Neural Interfaces with Photopatternable, Bioadhesive, and Highly Conductive Hydrogels for Stable Chronic Neuromodulation. *ACS Nano*, **17**, 885-895 (2023).

21. Y. Jiang *et al.*, Topological supramolecular network enabled high-conductivity, stretchable organic bioelectronics. *Science* **375**, 1411-1417 (2022).

22. Z. Jiang *et al.*, A 1.3-micrometre-thick elastic conductor for seamless on-skin and implantable sensors. *Nat. Electron.* **5**, 784-793 (2022).

23. J. Deng *et al.*, Electrical bioadhesive interface for bioelectronics. *Nat. Mater.* **20**, 229-236 (2021).

24. J. Kang *et al.*, Tough-interface-enabled stretchable electronics using non-stretchable polymer semiconductors and conductors. *Nat. Nanotechnol.* **17**, 1265-1271 (2022).

25. D. Song *et al.*, An Ultra-Thin MXene Film for Multimodal Sensing of Neuroelectrical Signals with Artifacts Removal. *Adv. Mater.* **35**, 2304956 (2023).

26. J. M. Lee *et al.*, The ultra-thin, minimally invasive surface electrode array NeuroWeb for probing neural activity. *Nat. Commun.* **14**, 7088 (2023).

27. R. A. Nawrocki *et al.*, Self-Adhesive and Ultra-Conformable, Sub-300 nm Dry Thin-Film Electrodes for Surface Monitoring of Biopotentials. *Adv. Funct. Mater.* **28**, 1803279 (2018).

28. X. Du *et al.*, Transparent and Stretchable Graphene Electrode by Intercalation Doping for Epidermal Electrophysiology. *ACS Appl. Mater. Interfaces* **12**, 56361-56371 (2020).

29. M. Ramezani *et al.*, High-density transparent graphene arrays for predicting cellular calcium activity at depth from surface potential recordings. *Nat. Nanotechnol.* (2024). https://doi.org/10.1038/s41565-023-01576-z

30. A. Savchenko *et al.*, Graphene biointerfaces for optical stimulation of cells. *Sci. Adv.* **4**, eaat0351 (2018).

31. Z. Lin *et al.*, Graphene Biointerface for Cardiac Arrhythmia Diagnosis and Treatment. *Adv. Mater.* **35**, 2212190 (2023).

32. H. Jang *et al.*, Graphene e-tattoos for unobstructive ambulatory electrodermal activity sensing on the palm enabled by heterogeneous serpentine ribbons. *Nat. Commun.* **13**, 6604 (2022).

33. S. Bhattacharya *et al.*, A Chest-Conformable, Wireless Electro-Mechanical E-Tattoo for Measuring Multiple Cardiac Time Intervals. *Adv. Electron. Mater.* **9**, 2201284 (2023).

34. Y. Zhao *et al.*, Ultra-conformal skin electrodes with synergistically enhanced conductivity for long-time and low-motion artifact epidermal electrophysiology. *Nat. Commun.* **12**, 4880 (2021).

35. S.-M. Kim *et al.*, Influence of PEDOT:PSS crystallinity and composition on electrochemical transistor performance and long-term stability. *Nat. Commun.* **9**, 3858 (2018).

36. X. Li *et al.*, Deciphering the superior thermoelectric property of post-treatment-free PEDOT:PSS/IL hybrid by X-ray and neutron scattering characterization. *npj Flexible Electron.* **6**, 6 (2022).

37. R. R. Jones, D. C. Hooper, L. Zhang, D. Wolverson, V. K. Valev, Raman Techniques: Fundamentals and Frontiers. *Nanoscale Res. Lett.* **14**, 231 (2019).

38. Z. Chen *et al.*, Soft, bioresorbable, transparent microelectrode arrays for multimodal spatiotemporal mapping and modulation of cardiac physiology. *Sci. Adv.* **9**, eadi0757 (2023).

39. S. S. Srinivasan *et al.*, On prosthetic control: A regenerative agonist-antagonist myoneural interface. *Sci Robot* **2**, eaan2971 (2017).

40. S. Iravanian, J. J. Langberg, A review of bioelectrodes for clinical electrophysiologists. *Heart Rhythm* **16**, 460-469 (2019).

41. M. A. Hasnul, N. A. A. Aziz, S. Alelyani, M. Mohana, A. A. Aziz, Electrocardiogram-Based Emotion Recognition Systems and Their Applications in Healthcare-A Review. *Sensors (Basel, Switzerland)* **21**, 5015v (2021).

42. J. P. Lee *et al.*, Encoding of multi-modal emotional information via personalized skin-integrated wireless facial interface. *Nat. Commun.* **15**, 530 (2024).

43. R. Y. Cai, A. L. Richdale, M. Uljarevic, C. Dissanayake, A. C. Samson, Emotion regulation in autism spectrum disorder: Where we are and where we need to go. *Autism Research* **11**, 962-978 (2018).

44. R. L. Zhou, S. Q. Hu, Effects of viewing pleasant and unpleasant photographs on facial EMG asymmetry. *Percept. Motor Skills* **99**, 1157-1167 (2004).

45. A. J. Fridlund, J. T. Cacioppo, GUIDELINES FOR HUMAN ELECTROMYOGRAPHIC RESEARCH. *Psychophysiology* **23**, 567-589 (1986).